Monthly Notices
of the
ROYAL ASTRONOMICAL SOCIETY

MNRAS **455,** 2345–2362 (2016) doi:10.1093/mnras/stv2424

Integral field spectroscopy of massive young stellar objects in the N113 H II region in the Large Magellanic Cloud

J. L. Ward,[1⋆] J. M. Oliveira,[1] J. Th. van Loon[1] and M. Sewiło[2,3]

[1]*School of Physical and Geographical Sciences, Lennard-Jones Laboratories, Keele University, Keele ST5 5BG, UK*
[2]*Space Science Institute, 4750 Walnut Street, Suite 205, Boulder, CO 80301, USA*
[3]*Department of Physics and Astronomy, The John Hopkins University, 366 Bloomberg Center, 6400N. Charles Street, Baltimore, MD 21218, USA*

Accepted 2015 October 19. Received 2015 September 11; in original form 2015 May 8

ABSTRACT

The *Spitzer* Surveying the Agents of Galaxy Evolution (SAGE) survey has allowed the identification and analysis of significant samples of Young Stellar Object (YSO) candidates in the Large Magellanic Cloud (LMC). However, the angular resolution of *Spitzer* is relatively poor meaning that at the distance of the LMC, it is likely that many of the *Spitzer* YSO candidates in fact contain multiple components. We present high-resolution *K*-band integral field spectroscopic observations of the three most prominent massive YSO candidates in the N113 H II region using Very Large Telescope/Spectrograph for INtegral Field Observations in the Near Infrared (VLT/SINFONI). We have identified six *K*-band continuum sources within the three *Spitzer* sources and we have mapped the morphology and velocity fields of extended line emission around these sources. Br γ, He I and H_2 emission is found at the position of all six *K*-band sources; we discuss whether the emission is associated with the continuum sources or whether it is ambient emission. H_2 emission appears to be mostly ambient emission and no evidence of CO emission arising in the discs of YSOs has been found. We have mapped the centroid velocities of extended Br γ emission and He I emission and found evidence of two expanding compact H II regions. One source shows compact and strong H_2 emission suggestive of a molecular outflow. The diversity of spectroscopic properties observed is interpreted in the context of a range of evolutionary stages associated with massive star formation.

Key words: circumstellar matter – stars: formation – stars: protostars – Magellanic Clouds – infrared: stars.

1 INTRODUCTION

The Large Magellanic Cloud (LMC) presents a unique opportunity to study star formation. At a distance of ∼50 kpc (Laney, Joner & Pietrzyński 2012) and a favourable inclination, it allows the simultaneous study of star formation on the scale of an entire galaxy and the scale of individual stars with little distance ambiguity. At the same time the LMC provides a 'stepping stone' towards understanding star formation in lower metallicity environments with a metallicity of $Z_{\rm LMC} \approx 0.4 Z_{\odot}$ (Dufour, Shields & Talbot 1982; Bernard et al. 2008).

The *Spitzer* Space Telescope (*Spitzer*; Werner et al. 2004) and the *Herschel* Space Observatory (*Herschel*; Pilbratt et al. 2010) have allowed the identification and characterization of the stellar populations in the LMC through the *Spitzer* SAGE ('Surveying the Agents of Galaxy Evolution'; Meixner et al. 2006) and the *Herschel* HERITAGE ('*Herschel* Inventory of the Agents of Galaxy Evolution'; Meixner et al. 2010, 2013) surveys. These surveys covered the whole of the LMC at 3.6, 4.5, 5.8, 8.0, 24, 70 and 160 μm (SAGE) and at 100, 160, 250, 350 and 500 μm (HERITAGE). Over 2000 Young Stellar Object (YSO) candidates have been selected using *Spitzer* photometry by Whitney et al. (2008), Gruendl & Chu (2009) and Carlson et al. (2012), with spectroscopic analyses carried out in Shimonishi et al. (2008), Seale et al. (2009), Shimonishi et al. (2010), Oliveira et al. (2009), van Loon et al. (2010) and Woods et al. (2011). The spatial resolution of *Spitzer* observations ranges from 1.7 arcsec at 3.6 μm to 40 arcsec at 160 μm whilst those of *Herschel* range from 8.6 arcsec (100 μm) to 40.5 arcsec (500 μm). These resolutions are insufficient to distinguish between YSOs with separations less than ∼0.5 pc of each other at the distance of the LMC. The effect of this poor spatial resolution in *Spitzer* imagery is that many *Spitzer* sources classified as YSOs will in fact be multiple objects which may exhibit a wide range of characteristics. The physical properties of the sources based on the *Spitzer* data may apply to groups of objects rather than individual sources.

LHA 120-N113 (hereafter N113; Henize 1956) is an active star-forming region within the LMC which contains a number of *Spitzer*

⋆ E-mail: j.l.ward@keele.ac.uk

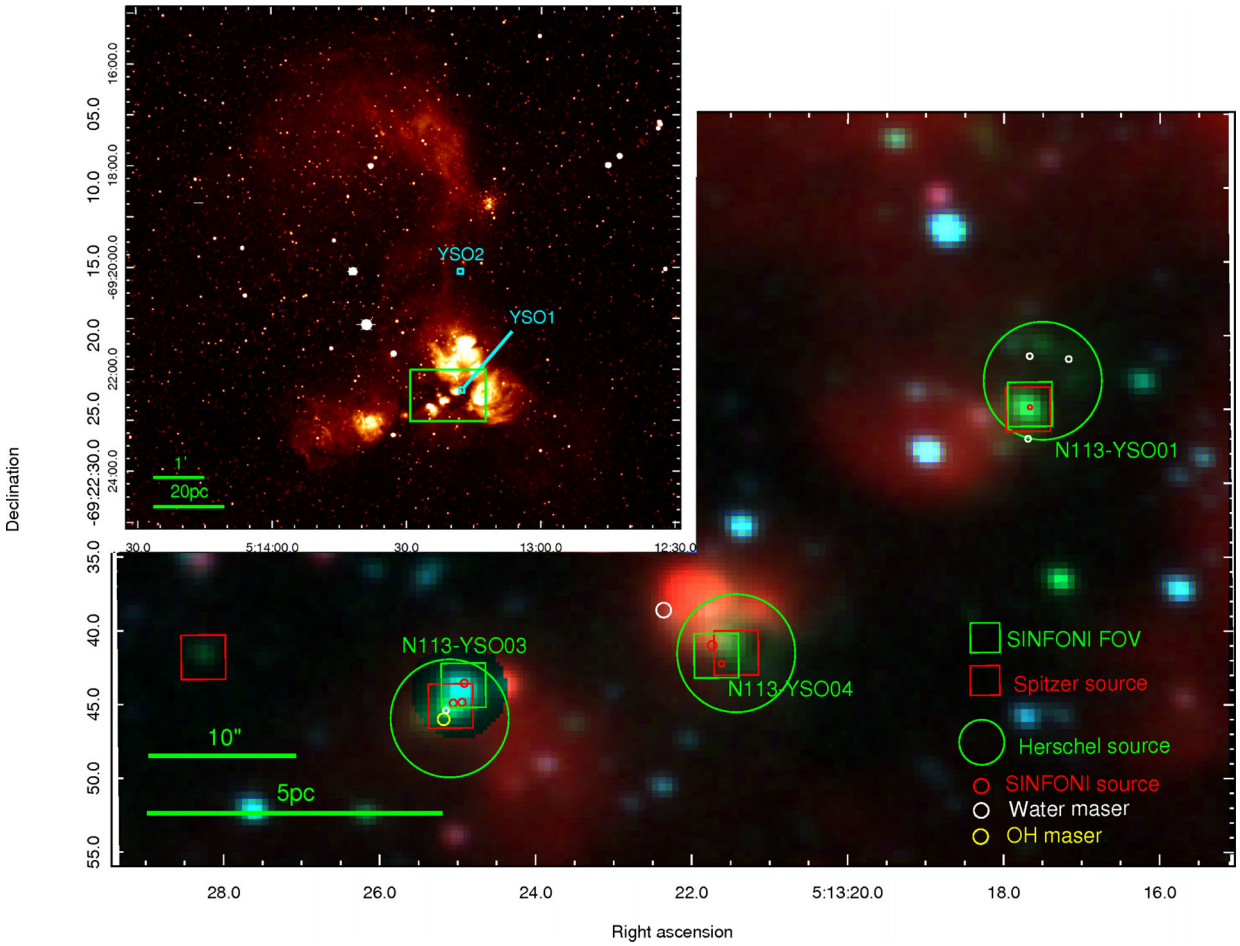

Figure 1. Top left-hand panel: wide field H α image[1] of N113 with positions of YSOs from Sewiło et al. (2010, cyan squares) and the region shown in the main image marked (green rectangle). Main image: three colour H α (red), IRSF *Ks*–band (green) and IRSF *H*–band (blue; Kato et al. 2007) composite showing positions of the observed N113 SINFONI FOVs (green squares) and YSO candidates identified in this work (red circles). Also included are the spectroscopically confirmed *Spitzer* YSOs (red squares), the *Herschel* YSO candidates (green circles; Seale et al. 2014), the water maser positions (white circles) and the position of the OH maser (yellow circle). The SINFONI red circles represent the region from which a spectrum was extracted for each continuum source whilst all other symbol sizes are representative of the spatial accuracy of the data.

and *Herschel* YSO candidate sources (see Fig. 1). We present *K*-band observations of three of the brightest *Spitzer* massive YSOs in N113 obtained with spectrograph for integral field observations in the near infrared (SINFONI; Eisenhauer et al. 2003) at the European Southern Observatory (ESO) Very Large Telescope (VLT), with spectral and spatial resolutions of 4000 and 0.1 arcsec, respectively. Sewiło et al. (2010) discussed two *Herschel* sources in N113 (YSO-1 and YSO-2, shown in Fig. 1) and two other YSOs (YSO-3 and YSO-4) in other regions of the LMC. To avoid confusion, we will retain the source numbers for YSO-1 and YSO-2 from Sewiło et al. (2010) but add the prefix N113- (N113-YSO01 and N113-YSO02) and add two additional YSOs in N113 (N113-YSO03 and N113-YSO04).

In order to compare the massive YSO population of N113 with that of the Milky Way, we require a suitable Galactic data set. The Red MSX[2] Source Survey (RMS Survey; Lumsden et al. 2013) provides the most comprehensive catalogue of Galactic massive YSOs and Ultracompact H II regions to date. *H*- and *K*-band infrared spectroscopy has been carried out for a large number of these objects by Cooper et al. (2013, henceforth C13). This Galactic sample will be used as a comparison for our LMC YSO observations.

Whilst *Spitzer* and *Herschel* observations provide a valuable insight into star formation in the Magellanic Clouds, shorter wavelength studies in the near-infrared using large ground-based telescopes allow us to resolve individual hot cores and compact H II regions at the distance of the LMC. These new observations provide the highest resolution imaging of these objects to date and the first *K*-band spectroscopy of massive YSOs in this region. Parameters determined from previous observations are presented in Section 2. Section 3 describes the observations and data reduction process, Section 4 presents the main results and finally, the significance and implications of the results are discussed in Section 5, along with efforts to place the observed targets into an evolutionary context.

2 PREVIOUS OBSERVATIONS

All three target regions (N113-YSO01, N113-YSO03 and N113-YSO04) are associated with bright knots in H α emission and have been previously studied using *Spitzer* photometry (Gruendl

[1] mosaic H α image of N113 from 'Magellanic Cloud Emission Line Survey 2' (PI: You-Hua Chu, http://adsabs.harvard.edu/abs/2011noao.prop..537C).
[2] Midcourse Space Experiment (Price et al. 2001).

Table 1. Properties of *Spitzer* YSOs analysed in this paper. YSO02 has been included for completeness using the values from Sewiło et al. (2010). The value for envelope mass is not included in Sewiło et al. (2010). The S09 group refers to the YSO classifications by Seale et al. (2009; S09) where P-type sources show prominent PAH emission, PE sources show strong PAH and fine-structure emission. All three of the targets observed in this work have been classed as definite YSOs by Gruendl & Chu (2009) and by Carlson et al. (2012). The bolometric luminosities and masses for N113-YSO01, N113-YSO03 and N113-YSO04 are from new SED fits using existing photometry (see the text for full details).

Target	*Spitzer* source	S09 group	$\log(L_{bol}/L_{\odot})$	Central mass ($M_{\odot}$)	Envelope mass ($M_{\odot}$)	Associated maser emission
N113-YSO02			$4.51^{+0.29}_{-0.30}$	13 ± 2		
N113-YSO01	Y051317.69−692225.0	PE	$5.18^{+0.18}_{-0.08}$	$32.3^{+0.3}_{-0.7}$	$1.8^{+6.3}_{-0.2} \times 10^2$	H_2O
N113-YSO03	Y051325.09−692245.1	P	$5.27^{+0.28}_{-0.27}$	$35.3^{+12.8}_{-0.9}$	$1.6^{+2.3}_{-1.1} \times 10^2$	H_2O, OH
N113-YSO04	Y051321.43−692241.5	PE	$5.24^{+0.31}_{-0.51}$	$34.3^{+13.9}_{-15.8}$	$1.2^{+33.3}_{-0.6} \times 10^2$	H_2O

& Chu 2009; Carlson et al. 2012), *Spitzer*-IRS spectroscopy (Seale et al. 2009), *Herschel* photometry (Sewiło et al. 2010) and *Herschel* spectroscopy (Oliveira et al., in preparation), confirming the YSO classification. Additionally, the region contains a number of water masers including the most intense in the Magellanic Clouds (Lazendic et al. 2002; Oliveira et al. 2006; Imai et al. 2013) and an OH maser (Brooks & Whiteoak 1997). None of the targets in this paper appear in the YSO catalogue of Whitney et al. (2008) because they do not satisfy the strict point source criterion of the original SAGE point source catalogue of Meixner et al. (2006); since the sources are absent from the SAGE catalogue they are not part of the YSO selection. This is most likely due to their slightly irregular morphologies and the issue is discussed in detail in Chen et al. (2009).

The following spectroscopic properties are common to all three targets: H_2 emission, polycyclic aromatic hydrocarbon (PAH) emission and fine-structure emission (from *Spitzer*-IRS spectra; Seale et al. 2009), and [C II] emission, [O I] emission, and CO emission (from *Herschel* Photoconductor Array Camera and Spectrometer (PACS) and Spectral and Photometric Imaging Receiver (SPIRE) spectroscopy; Oliveira et al. in preparation) whilst evidence of ices has not been observed in any of the targets. HCN and HCO^+ are also detected towards all three sources, indicating high densities (HCN and HCO^+) and photodissociation of molecular clouds (HCO^+), both of which are associated with massive star formation (Seale et al. 2012).

Additional properties, including results of spectral energy distribution (SED) fitting using the models of Robitaille et al. (2006), are summarized in Table 1. The SED fits for N113-YSO01, N113-YSO03 and N113-YSO04 are performed excluding the *Herschel* photometry and setting the *Spitzer* 70 μm data as upper limits because the spatial regions from which these data are extracted are too large to be directly useful when analysing individual YSOs. Physical parameters are estimated by averaging parameters of all models that fit a source's SED with normalized χ^2 per data point (χ^2/pt) in a range between $(\chi^2/pt)_{best}$ for the best-fitting model and $(\chi^2/pt)_{best} + 3$ (see e.g. Sewiło et al. 2013 for further details). The luminosity and mass of N113-YSO01 are consistent within the quoted uncertainties with those presented in Sewilo et al. (2010), fitted using all available photometry for $\lambda < 50$ μm. Using the calibration from Martins, Schaerer & Hillier (2005), the estimated luminosities would correspond to O4–O9 stars on the main sequence; however, such estimates cannot be taken at face value since at least two sources are actually resolved into multiple components in the *K*–band in this work. Whilst all three of the targets of this paper appear similar based on *Spitzer* and *Herschel* data, the *K*-band observations presented in this work reveal a wide range of sources with different spectral properties.

3 OBSERVATIONS AND DATA REDUCTION

K-band integral field spectroscopic observations were carried out for three targets in N113 using SINFONI at the VLT. SINFONI is an AO-assisted integral field spectrograph allowing for observations in the *K*–band with an angular resolution of 0.1 arcsec, a field of view (FOV) of 2.8 arcsec and a spectral resolving power, $R = \lambda/\delta\lambda = 4000$. These observations took place in 2013 October. Each object was observed with four 300 s integrations along with sky offset position observations in an ABBA pattern with jittering. Telluric B-type standard stars were also observed at regular intervals throughout each night in order to provide standard star spectra for telluric correction and flux calibration. Calibration frames were observed during the daytime and linearity lamp frames were obtained from the ESO archive.

The data were reduced using the standard SINFONI pipeline recipes with ESO's GASGANO data file organizer. Telluric and flux calibration were performed simultaneously for each cube using an IDL script written specifically for this task. For each pixel in the data cube, the target spectrum is divided by the telluric standard star spectrum removing the telluric absorption features. The target spectrum was then multiplied by a blackbody with a temperature based on the spectral type of the standard star used. The blackbody spectra used in this calibration were generated using PYRAF[3]. This process was looped to apply the same procedure to each spaxel in the cube.

SINFONI is a Cassegrain focus mounted instrument and as such it does suffer from a systematic time-dependent wavelength shift during each night due to flexure. This is always small (less than three resolution elements), therefore, it only presents an issue when determining accurate centroid velocity measurements. In order to account for this effect, a second wavelength calibration was performed on the final data cubes using the OH emission lines in the sky data cubes produced in the SINFONI data reduction pipeline.

Although sky line subtraction does form part of the standard SINFONI data reduction pipeline, due to the relatively long exposure times in this study (8 × 300 s exposures plus overheads), the variation in sky line intensities leads to sky line residuals remaining in the final data cubes. The positions of these residuals are shown in Fig. A2. Whilst aesthetically displeasing, the impact of these residuals on the spectral analysis is actually very small as none are coincident with any emission lines of interest and the continuum measurements are calculated from models fitted to the continuum.

[3] PYRAF is a product of the Space Telescope Science Institute, which is operated by AURA for NASA.

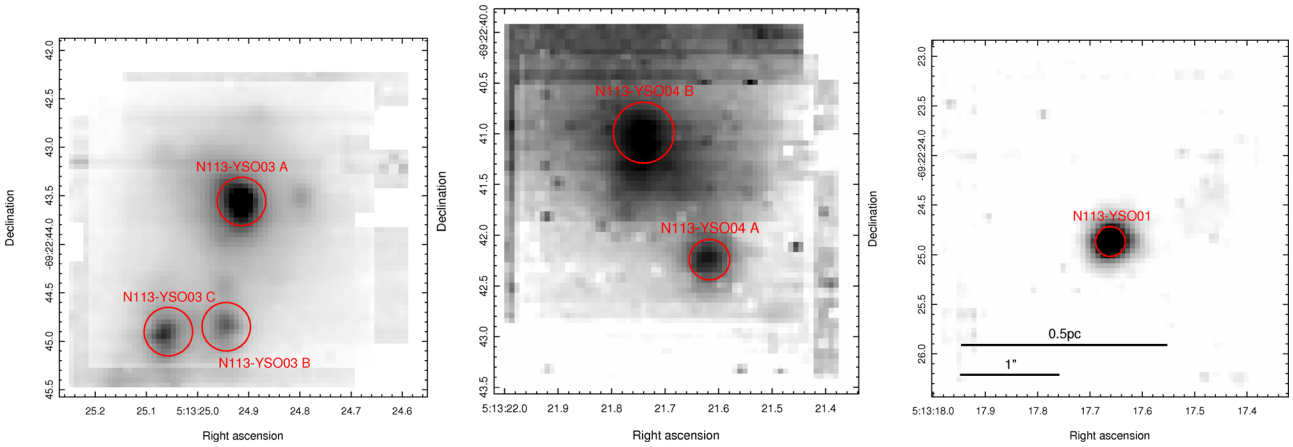

Figure 2. SINFONI *K*-band Continuum emission maps. Left to right: N113-YSO03, N113-YSO04 and N113-YSO01. Marked regions show the identified continuum sources and the regions from which spectra were extracted.

Table 2. J2000 positions of each of the *K*-band continuum sources resolved for the first time in this paper.

Object	RA (h:m:s)	Dec. (°:′:″)
N113-YSO01	05:13:17.666	−69:22:24.86
N113-YSO03 A	05:13:24.915	−69:22:43.55
N113-YSO03 B	05:13:24.944	−69:22:44.85
N113-YSO03 C	05:13:25.057	−69:22:44.90
N113-YSO04 A	05:13:21.617	−69:22:42.24
N113-YSO04 B	05:13:21.740	−69:22:40.99

4 RESULTS

4.1 Continuum emission and photometry

For each spaxel in the final flux calibrated cubes, the continuum was fitted using a third-order polynomial and summed for the spectral range spanning 2.028–2.290 μm to produce continuum flux maps without any contribution from line emission. The resulting images are shown in Fig. 2. Multiple continuum sources have been identified using these images; N113-YSO01 contains a single continuum source while N113-YSO03 and N113-YSO4 are resolved into three and two continuum sources, respectively. The positions of each continuum source are given in Table 2 and marked in Fig. 2 and the red circles show the regions from which 1D spectra were extracted from the cubes using the *sinfo_utl_cube2spectrum* recipe from the SINFONI data reduction pipeline (see Fig. A1 for extracted spectra). The *K*-band continuum magnitude for each object, integrated over the same wavelength interval, is given in Table 3.

4.2 Extinction

In order to impose constraints on the physical properties of the observed YSOs, we must apply extinction corrections to our measurements. Additionally, extinction towards an object can provide an assessment of how embedded the source of the emission is. We employed two methods of estimating the extinction towards each source. The first uses *JHKs* photometry from the Infrared survey facility (IRSF; Kato et al. 2007) and the same technique employed in C13:

$$A_V = \frac{m_1 - m_2 + x_{\rm int}}{0.55^{1.75}(\lambda_1^{-1.75} - \lambda_2^{-1.75})}, \quad (1)$$

where m_1 and m_2 are the shorter wavelength and longer wavelength magnitudes, respectively, and $x_{\rm int}$ is the intrinsic colour, assuming intrinsic colours of a B0 type star of 0.12 and 0.05 mag for $J-H$ and $H-K$, respectively.

The second method utilizes the H_2 line fluxes measured from the spectra themselves to estimate extinction. The 1–0Q(3)/1–0S(1) flux ratio is used due to its insensitivity to temperature and relatively large wavelength baseline. Following Davis et al. (2011), A_V is calculated as

$$A_V = -114 \log(0.704[I_{S1}/I_{Q3}]). \quad (2)$$

All the resulting extinction estimates are shown in Table 3. We find that the extinction estimates using the IRSF colours are inconsistent between $J-H$ and $H-K$ colours for the same source and for nearby objects in the same FOV. Additionally, the technique using IRSF photometry has yielded negative values, likely caused by source confusion and unreliable photometry in the relatively

Table 3. Measured *K*-band magnitudes and extinction estimates (calculated using both methods discussed in Section 4.2) for all observed continuum sources. The average for each SINFONI FOV is given in the last column. For N113-YSO04 only one IRSF source is detected and it is unclear which of the sources in this work corresponds to.

Target	*K*-band mag	A_V ($J-H$)	A_V ($H-Ks$)	A_V (H_2 1–0 S(1)/Q(3))	FOV average
N113-YSO01	16.27 ± 0.01	10.7 ± 1.2	16.1 ± 1.1	24.1 ± 17.3	24.1 ± 17.3
N113-YSO03 A	14.60 ± 0.03	−6.1 ± 2.4	−1.6 ± 3.3	13.5 ± 8.5	15.0 ± 0.8
N113-YSO03 B	15.45 ± 0.03	1.8 ± 1.3	11.8 ± 1.0	15.7 ± 5.4	15.0 ± 0.8
N113-YSO03 C	15.20 ± 0.01	8.9 ± 1.4		15.8 ± 3.9	15.0 ± 0.8
N113-YSO04 A	17.67 ± 0.03		11.6 ± 1.6	37.8 ± 8.9	32.4 ± 5.5
N113-YSO04 B	16.53 ± 0.06		11.6 ± 1.6	26.9 ± 6.5	32.4 ± 5.5

low-resolution IRSF data or by the assumption of spectral type. Wherever extinction corrections are applied, we use the values calculated using the H_2 lines as this technique makes no assumptions of intrinsic spectral type and it is available for all six sources. Using the Galactic mean R_V-dependent extinction law,

$$[A(\lambda)/A_V] = a(x) + b(x)/R_V, \quad (3)$$

where $a(x) = 0.574x^{1.61}$ and $b(x) = -0.527x^{1.61}$ for the *K*–band (Cardelli, Clayton & Mathis 1989), we calculated extinction corrections for all measured emission lines. The R_V value adopted is the same as that of the Milky Way extinction curve ($R_V = 3.1$). Although the average value in the LMC has been found to be $R_V = 3.41 \pm 0.06$ (Gordon et al. 2003), in the *K*–band the effect of a small variation in R_V is negligible when compared to the effect of the line measurement uncertainties.

4.3 Emission features

Emission-line mapping was achieved by fitting Gaussian profiles to the spectral axis in the final data cubes to calculate a line flux for each spaxel using our IDL script written for this task. The resulting images are shown in Fig. 3. Spectra were extracted from the regions shown in Fig. 2 of the flux-calibrated data cubes using the *sinfo_utl_cube2spectrum* recipe from the SINFONI data-reduction pipeline. Emission lines in the extracted 1D spectra for each continuum source were measured by Gaussian fitting within the STARLINK software package SPLAT. The measured emission-line fluxes (without extinction correction) are given in Table B1. The flux values obtained from the spectra were converted to line luminosities using a distance of 49.4 ± 0.5 kpc (Laney et al. 2012).

4.3.1 H I emission

The strongest detected H I emission line in this sample, Br γ, is most commonly associated with accretion in star formation studies. For intermediate-mass YSOs, the relation from Calvet et al. (2004) can be used to estimate the accretion luminosity from Br γ luminosity:

$$\log(L_{\rm acc}) = -0.7 + 0.9(\log(L_{{\rm Br}\,\gamma}) + 4). \quad (4)$$

Whilst this relation holds true for Herbig A stars, some of the higher mass Herbig B type stars have been observed to exhibit a Br γ emission excess (Donehew & Brittain 2011; Mendigutía et al. 2011), most likely due to an additional emission component originating from the strong winds driven by stellar ultraviolet photons emitted from hot stars. It is likely therefore that a similar effect is present in the more massive YSOs during the later phases of their evolution. For the purposes of comparing our sample with a Galactic sample, however, the above relation can be applied to gain an equivalent accretion luminosity assuming that both samples cover the same range of evolutionary states and YSO masses. Additionally, we must consider the impact that metallicity may have on this relation. Whilst it is the case that the momentum and mass-loss rates of stellar winds are strongly affected by metallicity (Vink, de Koter & Lamers 1999, 2001; Puls, Springmann & Lennon 2000; Kudritzki 2002; Krtička 2006), it is the number of photons produced which are able to ionize hydrogen that is significant when measuring Br γ emission. Kudritzki (2002) predicts that the number of photons capable of ionizing hydrogen is barely affected by a change in metallicity. This suggests that the above relationship between Br γ and accretion luminosity should hold for studies in lower metallicity environments.

Whilst bolometric luminosities have been obtained for each target using existing *Spitzer* data (see Table 1), two out of three target fields contain multiple continuum sources and the third exhibits emission that appears to originate from outside the FOV. Without higher resolution mid-infrared studies, it will not be possible to accurately determine bolometric luminosities for each of the sources. We therefore compare the equivalent accretion luminosity with *K*-band magnitude in Fig. 4 rather than bolometric luminosity. A distance of 49.4 ± 0.5 kpc (Laney et al. 2012) was assumed to the LMC and distances to Galactic sources were obtained from the RMS survey data base[4]. From Fig. 4, we can ascertain that the Br γ luminosities observed towards all six sources fall within the range observed in the Galactic sources. The sources for which we believe that the emission is associated with that source exhibit a higher Br γ/*K*-band continuum emission ratio than the remaining sources. The accretion rates of the YSOs in this study are consistent with those of Galactic YSOs but appear to be high, possibly indicative of higher accretion rates.

The spatial extent of the Br γ emission is mapped in the top row of Fig. 3. Where the Br γ emission is significantly spatially extended beyond the continuum source, it is likely that the contribution of non-accretion emission is significant. This appears to be the case in N113-YSO03 A and N113-YSO04 B. The Br γ emission is compact in N113-YSO03 B whilst in the remaining three continuum sources (N113-YSO01, N113-YSO03 C and N113-YSO04 A), the Br γ emission appears to be ambient or produced from other sources in the FOV. The dominant source of Br γ emission in N113-YSO01 peaks outside of the FOV.

In addition to mapping the Br γ emission flux around these sources, we have also mapped the centroid velocities relative to the centroid at the westernmost continuum source in each field (N113-YSO01, N113-YSO03 A and N113-YSO04 A), shown in Fig. 5. Spaxels where the uncertainty in relative velocity exceeds the imposed limits (5 km s^{-1} in YSO03 and 10 km s^{-1} in YSO01 and YSO04) have been masked. Fig. C1 shows emission-line velocity maps obtained from the sky cube for N113-YSO03, showing that there are no significant systematic velocity gradients. The two sources which exhibit extended Br γ emission (N113-YSO03 A and N113-YSO04 B) exhibit clear velocity gradients (±10 and ±5 km s^{-1}, respectively) centred on the continuum source, suggesting the expansion of excited gas around these objects. The off-source Br γ emission in the N113-YSO01 FOV appears to be slightly blueshifted with respect to the central continuum source.

The Pfund series is detected towards three of the six sources resolved in this work; N113-YSO03 A, N113-YSO03 B and N113-YSO04 B. Unfortunately, the *K*-band Pfund series lies in an area of poor atmospheric transmission, therefore, it is not easy to obtain accurate measurements of their flux. The positions of the detected Pfund series emission lines are shown in Fig. A3 and the measured line fluxes are listed in Table B1. Using the Pfund series emission and the Br γ emission, it is possible to obtain temperatures from the ratios of hydrogen recombination lines if the density is well constrained. Whilst the measured line ratios are certainly consistent with the presence of massive OB-type stars, no further constraints on these physical parameters were obtained from our data, due the low signal-to-noise (S/N) ratio in the Pfund series measurements, the large reddening uncertainties and the strong dependence on density that is poorly constrained.

[4] http://rms.leeds.ac.uk/cgi-bin/public/RMS_DATABASE.cgi; Lumsden et al. (2013)

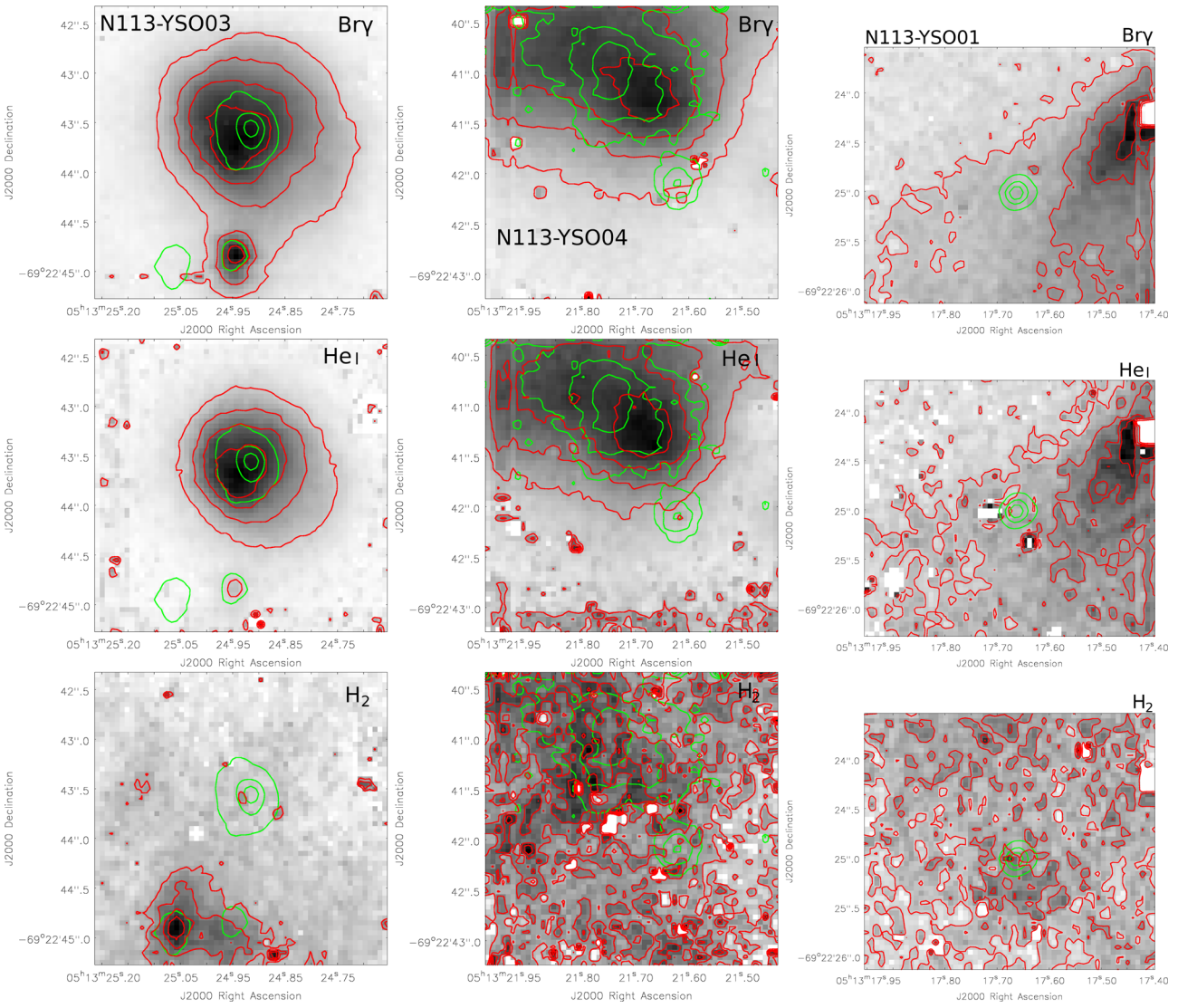

Figure 3. Emission-line maps with contours overlaid. Red contours – line emission [0.2, 0.4, 0.6, 0.8] × peak, green contours – continuum emission [0.25, 0.5, 0.75] × peak. Left to right – N113-YSO03, N113-YSO04, N113-YSO01. Top to bottom – Br γ, He I, H_2 1–0S(1).

4.3.2 He I emission

The primary production mechanism for the He I emission line is the ionization and subsequent recombination of helium which becomes significant at the ionization boundary and potentially in the collision with surrounding medium (Porter, Drew & Lumsden 1998). Whilst the He I/Br γ ratio is sensitive to the temperature of the emitting regions, its heavy dependence on density means that it cannot be used as a robust diagnostic of temperature (Shields 1993).

We detect the 2.0587 μm He I emission line at the position of all six of the continuum sources and it is detected as extended emission around two sources (N113-YSO03 A and N113-YSO04 B; see Fig. 3, middle row). The two sources which exhibit the extended He I emission are the strongest He I emitters and those with the first and third highest Br γ fluxes, respectively. The He I doublet at 2.113 μm was detected but not resolved towards three sources (N113-YSO03 A, N113-YSO04 A and N113-YSO04 B) indicating a collisional-excitation component in regions of high density (Lumsden, Puxley & Hoare 2001). The flux of the 2.113 μm doublet is typically significantly lower than the 2.058 μm line (Table B1) and the S/N for the doublet in our sample prevents further analysis. No He II emission has been detected towards any of the sources in this work.

Spatially, the He I emission tends to trace the same structures as the Br γ emission, although with weaker and slightly more compact emission. This is to be expected in sources where the central source is hot enough to excite a large volume of surrounding gas as in a compact H II region. In N113-YSO03 C and N113-YSO04 A, the detected He I emission appears to be ambient to the region, possibly originating from N113-YSO03 A and N113-YSO04 B, respectively. The He I emission in N113-YSO01 traces the morphology of the Br γ emission, also appearing to originate outside of the FOV.

Fig. 6 plots the He I 2.0587 μm emission-line luminosity against the Br γ luminosity for all N113 continuum sources and those from C13 for which both line measurements are available. It appears that the same trend and range of values is observed in N113 as in the Milky Way. The off-source emission in N113-YSO01 (indicated by '1 ext') appears to have a comparable He I/Br γ ratio to

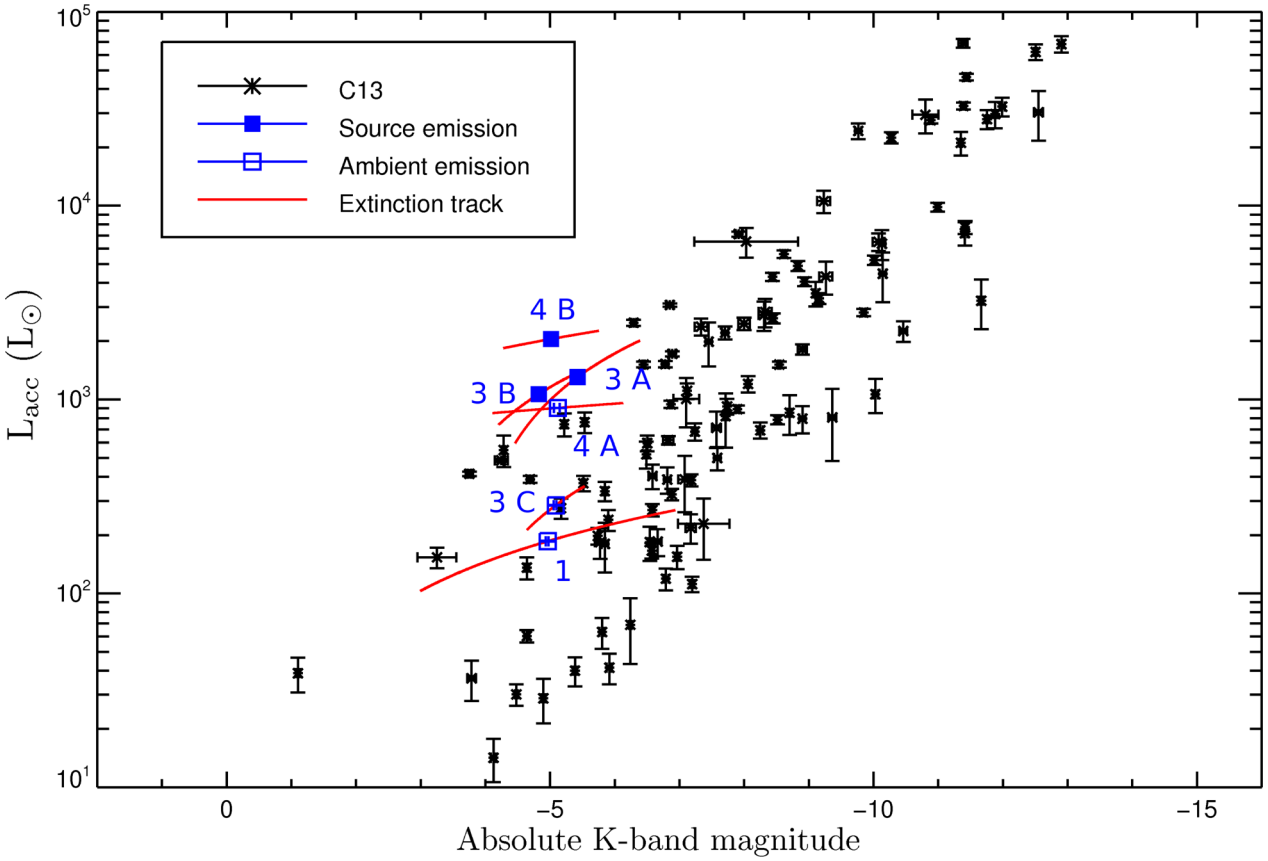

Figure 4. Equivalent accretion luminosity against absolute *K*-band magnitudes. A distance to the LMC of 49.4 ± 0.5 kpc is assumed. Extinction correction has been applied using A_V values described in Section 4.2 for the N113 data and A_V values from C13 for the Galactic data. Slit losses have not been taken into account for the Galactic data. The range of possible values allowed by the uncertainty in extinction for each N113 source is shown as a red extinction track. For clarity, the N113-YSO prefixes have been omitted. Source emission (filled squares) and ambient emission (open squares) are discussed in the main text.

N113-YSO03 A and N113-YSO04 B, suggesting that it presents a relatively energetic environment.

As well as tracing the same morphological structures, where extended He I emission is present it exhibits the same velocity fields as the Br γ emission, as demonstrated in Fig. 5 for N113-YSO03 and N113-YSO04. This is further evidence that the extended Br γ emission and extended He I emission originate from the same strong radiation field.

4.3.3 H_2 emission

The H_2 lines detected in our spectra are identified in Fig. A1. Although the H_2 emission has been spatially mapped (see Fig. 3), the S/N per spaxel in N113-YSO01 and N113-YSO04 for the H_2 lines is poor and very little morphological information can be obtained. Additionally, it appears likely that the H_2 emission in N113-YSO01 and N113-YSO04 is consistent with uniform ambient H_2 emission, unrelated to the discrete YSOs. In N113-YSO03, the H_2 emission is relatively compact and peaks at the position of source C. The H_2 emission measured in source B may have a significant component originating from source C. Whilst N113-YSO03 A does not show significant H_2 emission in Fig. 3, on inspection of the extracted spectrum it does exhibit relatively weak H_2 emission which is likely to be ambient, as is the case for N113-YSO01 and N113-YSO04. In summary, only N113-YSO03 C is a significant source of H_2 emission.

The H_2 2.1218 μm emission luminosity is plotted against the Br γ luminosity for each of the continuum sources in Fig. 7. Little correlation can be seen on this diagram, suggesting that the emitting regions of the lines are unrelated. N113-YSO03 C clearly falls above the H_2 = Br γ line, whereas Br γ > H_2 for all of the other sources, indicating that N113-YSO03 C is dominated by H_2 emission whilst the remaining sources are dominated by atomic Br γ emission, consistent with the view that the H_2 emission in N113-YSO01, N113-YSO04 and possibly N113-YSO03 A is mostly ambient.

The ratios of *K*-band H_2 line fluxes can be used to determine whether the source of the emission is photodissociation or shock excited. The extinction corrected flux ratios for all of the observed H_2 lines with respect to the 1–0S(1) line are shown in Table 4, with the expected ratios based on models of photo-excited emission and interstellar shocks in molecular clouds at various temperatures given in the lower part of Table 4. Whilst it is likely that all targets have contributions from both shocked and a photodissociation region (PDR), we can use these values to determine which excitation mechanism of H_2 emission is dominant. In the radiative excitation scenario, the ratios with respect to the 2.1218 μm 1–0S(1) line should fall in the range 0.5–0.6 and 0.4–0.7 for the 2–1S(1) and 1–0S(0) lines (at 2.2477 μm and 2.2235 μm), respectively (Black & van Dishoeck 1987). Adopting T = 2000 K, shock excitation should give values of 0.08 and 0.21, respectively, for the same emission-line ratios (Shull & Hollenbach 1978). Together, these two line ratios form a powerful diagnostic tool as the 2–1S(1) line ratio has a significant shock temperature dependance, whereas the 1–0S(0)

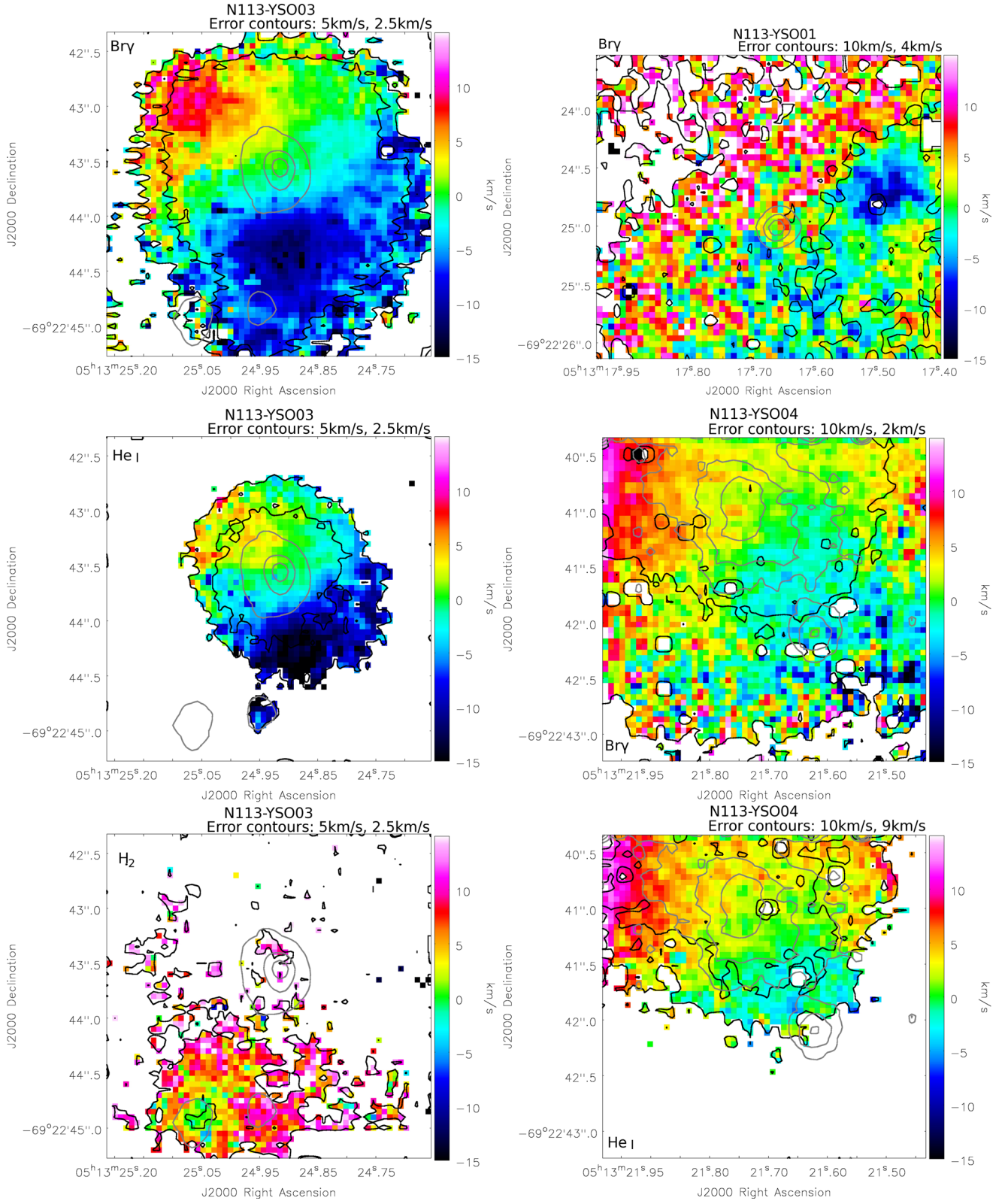

Figure 5. Left: Br γ, He I and H_2 2.1218 μm centroid velocity maps for N113-YSO03. Right: Br γ centroid velocity map for N113-YSO01 (top) and Br γ and He I velocity maps for N113-YSO04 (middle and bottom). Black contours represent the uncertainties; the outer (left) and inner (right) contour values are indicated in each image. The continuum contour levels are [0.25, 0.5, 0.75] × peak (grey).

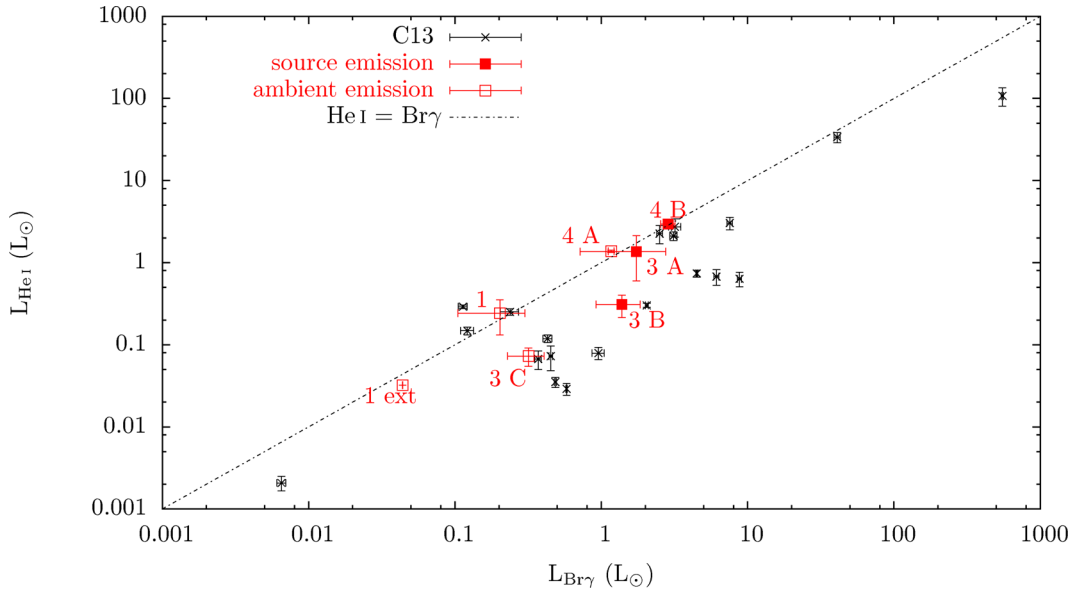

Figure 6. He I luminosity plotted against Br γ luminosity for all continuum sources. 1 ext denotes the extended emission in the N113-YSO01 cube (not corrected for extinction). For clarity the N113-YSO prefixes have been omitted.

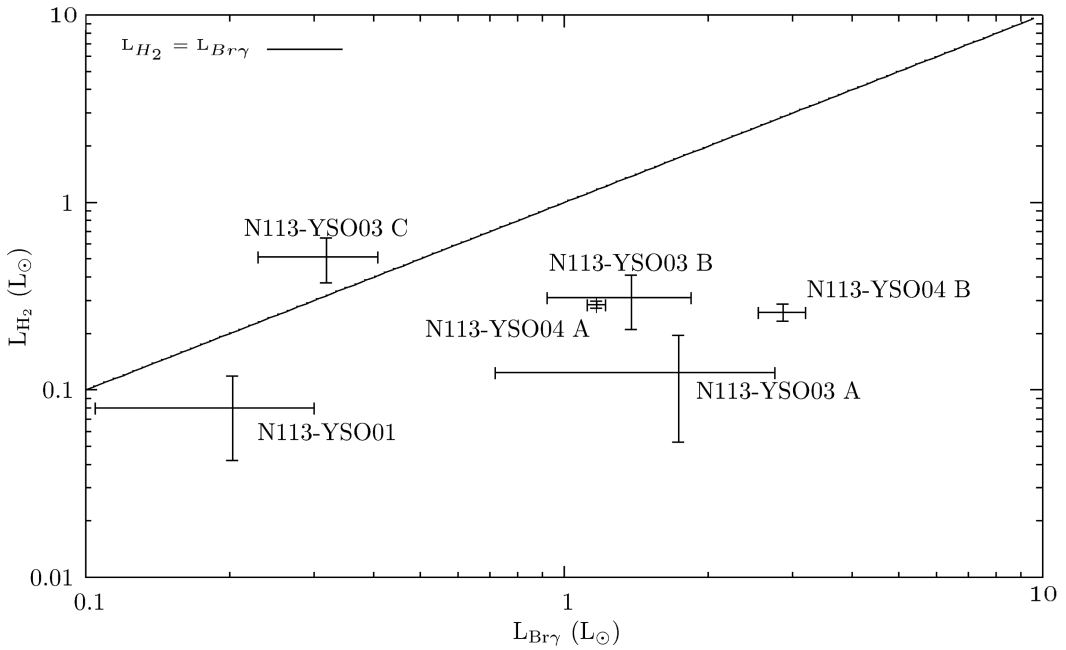

Figure 7. H_2 2.1218 μm emission against Br γ emission for all observed continuum sources.

ratio exhibits a large gap between predicted PDRs and shocks and, crucially, an inverse dependance on shock temperature.

In Fig. 8, we compare our observed 1–0S(0) and 2–1S(1) ratios relative to the 1–0S(1) line to those expected from photo-excitation, and shocked emission at 2000 and 4000 K. We find that in the upper panel, three sources appear highly likely to be shock emission dominated (N113-YSO03 C, N113-YSO04 A and N113-YSO04 B) and two sources could be PDR emission dominated (N113-YSO03 A and N113-YSO03 B), but the uncertainties are large and therefore they could also fall within the shocked regime. For the final source (N113-YSO01), the uncertainty in the 1–0S(0) flux is such that no conclusions can be drawn on the origin of the emission. In the lower panel of Fig. 8, all of the sources appear to fall within the shocked emission zone, with two of the sources (N113-YSO01 and N113-YSO03 A) within 1σ of PDR emission. From this we can draw the conclusion that for N113-YSO03C (the only source for which H_2 emission is not ambient) the emission is shock dominated. The H_2 emission from sources A and B in N113-YSO03 appears to have contribution from both shock excitation and photodissociation, whilst towards both sources in N113-YSO04 the emission appears to be shock dominated. Due to low S/N, no conclusion can be drawn for the source of the H_2 emission in N113-YSO01.

N113-YSO03 was the only source for which we were able to make H_2 centroid velocity measurements (Fig. 5) and over the relatively small spatial range where this was possible, there appears

Table 4. Extinction-corrected H_2 emission-line ratios with respect to the 1–0S(1) emission line for all objects. Also included are the expected H_2 line ratios for photodissociation (Black & van Dishoeck 1987) and shocked emission (Shull & Hollenbach 1978).

Object	1–0S(0) 2.2235 μm	1–0S(2) 2.0338 μm	1–0S(3) 1.9576 μm	2–1S(1) 2.2477 μm	2–1S(2) 2.1542 μm	2–1S(3) 2.0735 μm
N113-YSO01	0.31 ± 0.35	0.68 ± 0.57		0.39 ± 0.27	0.18 ± 0.12	
N113-YSO03 A	0.41 ± 0.34	0.36 ± 0.28	0.44 ± 0.35	0.30 ± 0.25	0.15 ± 0.12	0.34 ± 0.27
N113-YSO03 B	0.37 ± 0.18	0.30 ± 0.13	0.24 ± 0.10	0.17 ± 0.08	0.06 ± 0.03	0.21 ± 0.09
N113-YSO03 C	0.28 ± 0.11	0.34 ± 0.12	0.45 ± 0.16	0.15 ± 0.06	0.06 ± 0.02	0.17 ± 0.06
N113-YSO04 A	0.26 ± 0.02	0.46 ± 0.04		0.20 ± 0.02	0.15 ± 0.02	0.23 ± 0.02
N113-YSO04 B	0.26 ± 0.04	0.53 ± 0.09		0.34 ± 0.06	0.19 ± 0.03	0.40 ± 0.06
Photoexcitation	0.4–0.7	0.4–0.6		0.5–0.6	0.2–0.4	0.2–0.3
1000 K shock	0.27	0.27	0.51	0.005	0.001	0.003
2000 K shock	0.21	0.37	1.02	0.083	0.031	0.084
3000 K shock	0.19	0.42	1.29	0.21	0.086	0.27
4000 K shock	0.19	0.44	1.45	0.33	0.14	0.47

to be a small velocity gradient towards the red in the emission west of source C.

5 DISCUSSION

5.1 N113-YSO01

The N113-YSO01 FOV contains a single VLT *K*-band continuum source to a resolution of 0.2 arcsec. *Spitzer* resolution at the shortest wavelengths is ∼2 arcsec, therefore, whilst the bolometric luminosity ($1.51^{+0.78}_{-0.25} \times 10^5$ $L_\odot$) for this source is likely to be more robust, the emission lines from the spatially unresolved studies will likely be contaminated by the off-source emission seen in Fig. 3. Both the Br γ-emission and the He I-emission peak approximately 1.3 arcsec (∼0.31 pc) away from the continuum source. It appears that all of the measured line emission towards this object is ambient and if line emission from the source is present, it is too weak to be detected in this work. In the top panel of Fig. 1, two large H α bubbles can be seen in close proximity to N113-YSO01. Thus, it is possible that the line emission detected towards N113-YSO01 is associated with these larger scale structures.

Fig. 1 shows the positions of three maser sources that are close to N113-YSO01; however, spectroscopically N113-YSO01 does not exhibit any indicators of strong outflows which could stimulate the maser emission. Additionally, the distances (0.52–1.01 pc) between these masers and the N113-YSO01 infrared source suggests that the masers may be in fact associated with other, weaker *K*-band sources just visible in Fig. 1. The maser sources also do not appear to coincide with the prominent *Spitzer* source.

Massive YSOs without any significant *K*-band emission lines are not common in the Galactic data set but they have been observed (e.g. G103.8744+01.8558; C13). Longer wavelength data available for those Galactic sources makes the YSO identification credible. It is possible that such sources represent the youngest hot core objects or they are simply weakly emitting YSOs. However, the possibility that the source observed in the N113-YSO01 FOV is not in fact a YSO cannot be excluded by this work. At this stage, we are unable to constrain the origin of the line emission in the *K*-band and *Spitzer*-IRS spectra.

5.2 N113-YSO03

The line morphologies observed in the N113-YSO03 FOV suggest that the three continuum sources represent three different stages of star formation, likely reflecting a range of masses. N113-YSO03 A is the brightest of all the observed sources in the *K*–band with strong, extended and expanding Br γ emission and He I emission, implying that it is a relatively evolved compact H II region. It also has the strongest He I emission, likely caused by the strong winds associated with an emerging massive star.

N113-YSO03 B also exhibits strong Br γ emission, but it is compact and the He I emission is much weaker, suggesting a considerably lower contribution to the Br γ emission from an H II region and thus a cooler and likely earlier stage (younger or less massive) object than N113-YSO03 A, possibly dominated by accretion emission.

N113-YSO03 C exhibits very weak or absent Br γ and He I emission, and very strong H_2 emission. In addition, the H_2 line ratios are consistent with emission that is very heavily dominated by shocked emission with temperatures in the range 2000–3000 K. It is therefore likely that N113-YSO03 C is the least evolved of the three sources, representing an early stage YSO with strong bipolar outflows. This is also consistent with the much redder continuum slope for its spectrum. The highest intensity water maser source in the Magellanic Clouds was identified at a distance of 0.36 ± 0.07 pc (1.5 arcsec $\pm$ 0.3 arcsec) of source N113-YSO03 C (Lazendic et al. 2002; Oliveira et al. 2006; Carlson et al. 2012). Of the three sources resolved in this FOV, N113-YSO03 A is the most massive, having evolved to the point of shaping its environment in the form of a compact H II region, while N113-YSO03 C is the least evolved and thus the least massive.

5.3 N113-YSO04

N113-YSO04 exhibits two continuum sources, one compact and one extended and more diffuse. It is likely that most if not all of the H_2 emission detected in the FOV is ambient emission.

As in N113-YSO01, all of the emission in N113-YSO04 A appears to be either ambient emission (H_2 emission) or contaminating emission (Br γ and He I) from N113-YSO04 B. Therefore, the possibility that N113-YSO04 A is not a YSO cannot be excluded based on currently available data. N113-YSO04 A exhibits a considerably redder continuum than N113-YSO04 B (see Fig. A1) and a significantly higher A_V, indicating a more embedded object.

The extended source (N113-YSO04 B) shows strong Br γ and He I emission which is slightly offset from the continuum source. The underlying cause for the offset in the extended line emission is

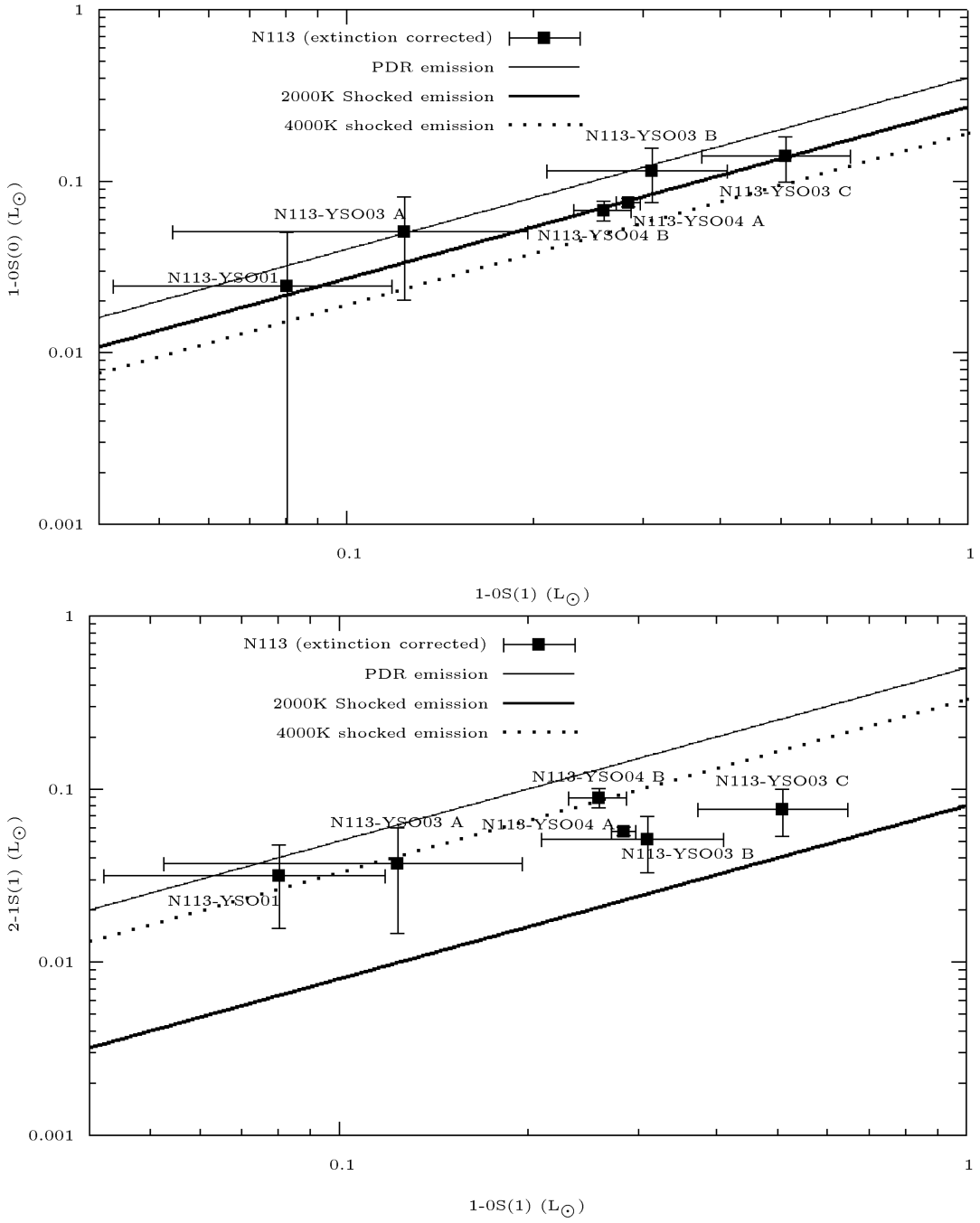

Figure 8. Top: H_2 1–0S(0) 2.2235 μm emission against H_2 1–0S(1) 2.1218 μm emission for all observed continuum sources. Bottom: H_2 2–1S(1) 2.2477 μm emission against H_2 1–0S(1) 2.1218 μm emission for all observed continuum sources. Lines shown are for photodissociation emission and shocked emission at 2000 and 4000 K as indicated in the legend.

unclear but it is likely to be a result of the geometry of the central source and its projection on to the sky. It also exhibits a similar expanding velocity profile for the Br γ and He I emission as N113-YSO03 A, implying that strong winds are present around both of these sources and that N113-YSO04 B is in a similar evolutionary state to N113-YSO03 A. The detection of the He I 2.113 μm doublet towards both sources is also consistent with an energetic, high-density region such as a compact H II region.

An H_2O maser has been previously identified to the north-east of this region (see fig. 1, Imai et al. 2013); however, it has a relatively large separation of 9.6 arcsec ± 0.5 arcsec (2.3 ± 0.1 pc), which would indicate that this maser is not likely to be associated with either of the N113-YSO04 sources.

6 SUMMARY AND CONCLUSIONS

Using the SINFONI integral field spectrograph at the VLT, we have observed a sample of three *Spitzer*-selected YSOs in the bright dusty lane in N113. The three targets look very similar at longer wavelengths: all are classified as P- or PE-type sources (*Spitzer*/IRS spectrum rich in PAH emission and fine-structure emission; Seale et al. 2009). When the sources are observed at higher resolution in

the *K*–band, a wide variety of morphological and spectral features is revealed. Our results are summarized below.

(i) Of the three *Spitzer* sources, six distinct *K*-band continuum sources have been resolved. N113-YSO01 contains only a single continuum source, N113-YSO03 contains three and N113-YSO04 contains two.

(ii) Two sources (N113-YSO03 A, N113-YSO04 B) exhibit strong, extended wind features and are therefore likely to be compact H II regions, i.e. massive objects in the final stages of star formation. The presence of the 2.113 μm He I emission suggests that these are indeed compact H II regions since in the C13 Galactic sample this doublet is only found towards H II regions.

(iii) N113-YSO03 C is dominated by H_2 emission, which is likely to occur in the collimated outflows driven by the youngest hot core phase objects.

(iv) N113-YSO03 B appears to be a fairly typical, massive YSO: a point source with strong Br γ emission and weaker He I emission.

(v) The remaining sources, N113-YSO01 and N113-YSO04 A, are compact and do not appear to have any emission lines associated with the continuum source (all observed line emission appears to be ambient). For N113-YSO04 A, this emission is likely to be sourced from the extended source N113-YSO04 B, whereas in N113-YSO01, the source of the line emission appears to be outside the FOV. Without additional data, it is unclear where either of these sources would fall in an evolutionary context: these objects could be featureless YSOs but the possibility of a non-YSO classification cannot be excluded.

(vi) Levels of extinction have been found to be typically lower than those within our Galaxy. The average extinction, A_V and standard deviation of our sample is 22.3 ± 9.3 mag compared with the values of C13 of 45.7 ± 17.6 mag. The average extinction towards massive YSOs in N113 is approximately half that of the Milky Way, consistent with the lower dust-to-gas ratio observed in the LMC (Bernard et al. 2008) and an LMC metallicity of approximately half solar metallicity.

(vii) A number of interstellar H_2O masers and a single OH maser have previously been detected in the region; however, many of these in fact fall at a significant distance from the continuum sources (>0.5 pc) and are therefore unlikely to be excited by the sources resolved here. The one exception is N113-YSO03 C which is likely to be the excitation source of the water maser to the south-east and also possibly the OH maser.

(viii) Emission line fluxes are similar to those found in the Milky Way but the detection rates of the He I 2.058 μm emission line are higher in this sample than in C13. However, this is only a small sample and it may include a higher proportion of later stage YSOs and compact H II regions compared to C13.

(ix) The equivalent accretion luminosities calculated are consistent with the Galactic distribution but appear to be high for their *K*-band magnitudes. The approach used here however does neglect any effects of metallicity *K*-band continuum emission.

(x) The CO bandhead, often associated with accretion discs in YSOs, is not detected in any of our sources. Even though the disc geometry can have a significant impact on the detection of CO (Kraus et al. 2000; Barbosa et al. 2003) and the sample is small, the lack of CO bandhead emission could be due to CO destruction in the harder radiation fields associated with lower metallicity environments.

(xi) Finally, we have mapped the velocity fields of extended gas structures around two of the continuum sources (N113-YSO03 A and N113-YSO04 B). These measurements imply stellar feedback in the form of stellar winds from newly formed massive stars at the centre of compact H II regions, driving expansion.

Through high-resolution characterization of three similar *Spitzer* sources, we have revealed a wide range of morphological and spectral properties. Two out of the three *Spitzer* sources in this study contain multiple YSOs and it is likely that this is not an uncommon occurrence in the Magellanic Clouds. Crucially, we have shown that whilst *Spitzer* and *Herschel* observations provide valuable insights into the star formation process in the Magellanic Clouds, higher spatial resolution is required in order to develop a full understanding of the YSOs in question, especially when comparing them to Galactic samples.

ACKNOWLEDGEMENTS

The authors thank the anonymous referee for his/her useful comments. JLW acknowledges financial support from the Science and Technology Facilities Council of the UK (STFC) via the PhD studentship programme. The authors would like to thank the staff at ESO's Paranal observatory for their support during the observations. This paper made use of information from the Red MSX Source survey data base at http://rms.leeds.ac.uk/cgi-bin/public/RMS_DATABASE.cgi which was constructed with support from STFC. This research has made use of the SIMBAD data base, operated at CDS, Strasbourg, France.

REFERENCES

Barbosa C. L., Damineli A., Blum R. D., Conti P. S., 2003, AJ, 126, 2411
Bernard J.-P. et al., 2008, AJ, 136, 919
Black J. H., van Dishoeck E. F., 1987, ApJ, 322, 412
Brooks K. J., Whiteoak J. B., 1997, MNRAS, 291, 395
Calvet N., Muzerolle J., Briceño C., Hernández J., Hartmann L., Saucedo J. L., Gordon K. D., 2004, AJ, 128, 1294
Cardelli J. A., Clayton G. C., Mathis J. S., 1989, ApJ, 345, 245
Carlson L. R., Sewiło M., Meixner M., Romita K. A., Lawton B., 2012, A&A, 542, A66
Chen C.-H. R., Chu Y.-H., Gruendl R. A., Gordon K. D., Heitsch F., 2009, ApJ, 695, 511
Cooper H. D. B. et al., 2013, MNRAS, 430, 1125 (C13)
Davis C. J. et al., 2011, A&A, 528, A3
Donehew B., Brittain S., 2011, AJ, 141, 46
Dufour R. J., Shields G. A., Talbot R. J., Jr, 1982, ApJ, 252, 461
Egan M. P. et al., 2003, Technical Report AFRL-VS-TR-2003-1589, Air Force Research Laboratory
Eisenhauer F. et al., 2003, in Iye M., Moorwood A. F. M., eds, Proc. SPIE Conf. Ser. Vol. 4841, Instrument Design and Performance for Optical/Infrared Ground-based Telescopes. SPIE, Bellingham, p. 1548
Gordon K. D., Clayton G. C., Misselt K. A., Landolt A. U., Wolff M. J., 2003, ApJ, 594, 279
Gruendl R. A., Chu Y.-H., 2009, ApJS, 184, 172
Henize K. G., 1956, ApJS, 2, 315
Imai H., Katayama Y., Ellingsen S. P., Hagiwara Y., 2013, MNRAS, 432, L16
Kato D. et al., 2007, PASJ, 59, 615
Kraus M., Krügel E., Thum C., Geballe T. R., 2000, A&A, 362, 158
Krtička J., 2006, MNRAS, 367, 1282
Kudritzki R. P., 2002, ApJ, 577, 389
Laney C. D., Joner M. D., Pietrzyński G., 2012, MNRAS, 419, 1637
Lazendic J. S., Whiteoak J. B., Klamer I., Harbison P. D., Kuiper T. B. H., 2002, MNRAS, 331, 969
Lumsden S. L., Puxley P. J., Hoare M. G., 2001, MNRAS, 328, 419
Lumsden S. L., Hoare M. G., Urquhart J. S., Oudmaijer R. D., Davies B., Mottram J. C., Cooper H. D. B., Moore T. J. T., 2013, ApJS, 208, 11

Martins F., Schaerer D., Hillier D. J., 2005, A&A, 436, 1049
Meixner M. et al., 2006, AJ, 132, 2268
Meixner M. et al., 2010, A&A, 518, L71
Meixner M. et al., 2013, AJ, 146, 62
Mendigutía I., Calvet N., Montesinos B., Mora A., Muzerolle J., Eiroa C., Oudmaijer R. D., Merín B., 2011, A&A, 535, A99
Oliveira J. M., van Loon J. T., Stanimirović S., Zijlstra A. A., 2006, MNRAS, 372, 1509
Oliveira J. M. et al., 2009, ApJ, 707, 1269
Pilbratt G. L. et al., 2010, A&A, 518, L1
Porter J. M., Drew J. E., Lumsden S. L., 1998, A&A, 332, 999
Price S. D., Egan M. P., Carey S. J., Mizuno D. R., Kuchar T. A., 2001, AJ, 121, 2819
Puls J., Springmann U., Lennon M., 2000, A&AS, 141, 23
Robitaille T. P., Whitney B. A., Indebetouw R., Wood K., Denzmore P., 2006, ApJS, 167, 256
Seale J. P., Looney L. W., Chu Y.-H., Gruendl R. A., Brandl B., Chen C.-H. R., Brandner W., Blake G. A., 2009, ApJ, 699, 150
Seale J. P., Looney L. W., Wong T., Ott J., Klein U., Pineda J. L., 2012, ApJ, 751, 42
Seale J. P. et al., 2014, AJ, 148, 124
Sewiło M. et al., 2010, A&A, 518, L73
Sewiło M. et al., 2013, ApJ, 778, 15
Shields J. C., 1993, ApJ, 419, 181
Shimonishi T., Onaka T., Kato D., Sakon I., Ita Y., Kawamura A., Kaneda H., 2008, ApJ, 686, L99
Shimonishi T., Onaka T., Kato D., Sakon I., Ita Y., Kawamura A., Kaneda H., 2010, A&A, 514, A12
Shull J. M., Hollenbach D. J., 1978, ApJ, 220, 525
van Loon J. T. et al., 2010, AJ, 139, 68
Vink J. S., de Koter A., Lamers H. J. G. L. M., 1999, A&A, 350, 181
Vink J. S., de Koter A., Lamers H. J. G. L. M., 2001, A&A, 369, 574
Werner M. W. et al., 2004, ApJS, 154, 1
Whitney B. A. et al., 2008, AJ, 136, 18
Woods P. M. et al., 2011, MNRAS, 411, 1597

APPENDIX A: EXTRACTED SPECTRA

Fig. A1 shows the 1D spectra extracted from the regions shown in Fig. 2 for all of the sources discussed in this paper. The emission-line identifications are marked on the spectra of N113-YSO03 C and N113-YSO01 with dotted lines showing the positions of the measured lines in all spectra. The positions of all significant sky emission-line residuals are marked on the spectrum of N113-YSO03 C in Fig. A2. Fig. A3 shows the positions of the Pfund series emission in the spectrum of N113-YSO03 A.

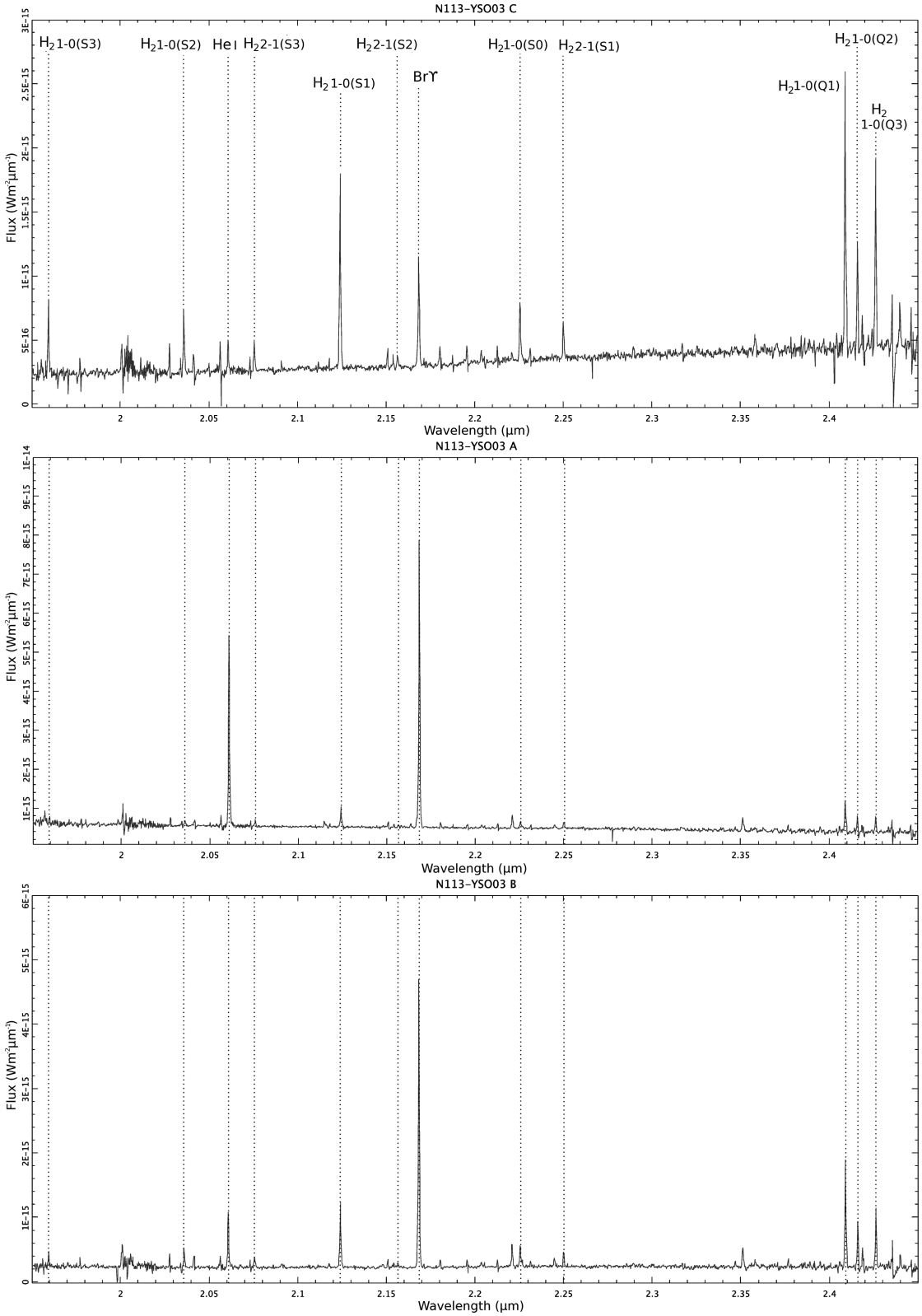

Figure A1. Spectra of all N113 continuum sources extracted from the regions shown in Fig. 2. The spectrum of N113-YSO03 C (shown first) is marked with the positions of all of the measured spectral lines.

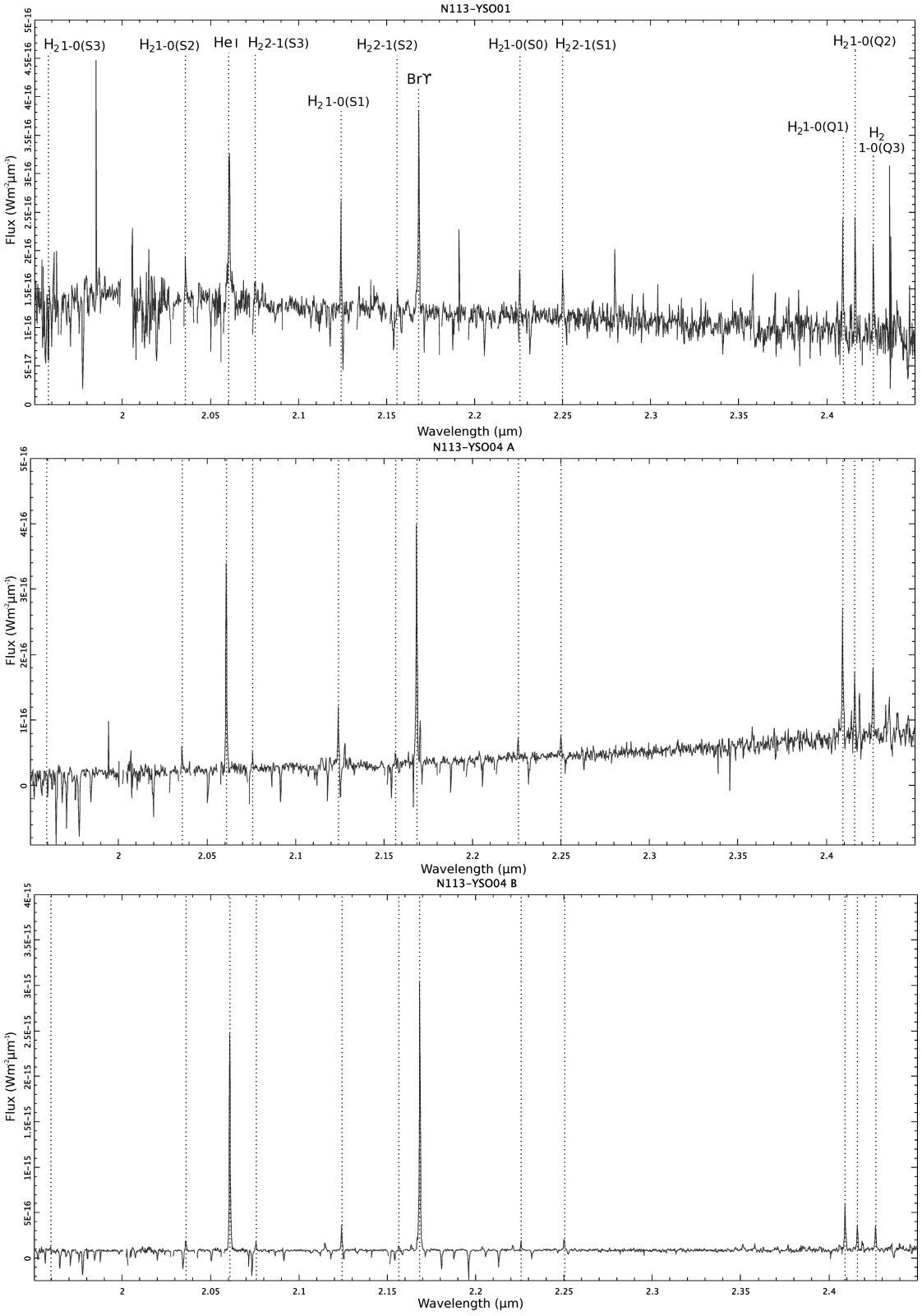

Figure A1 – *continued.*

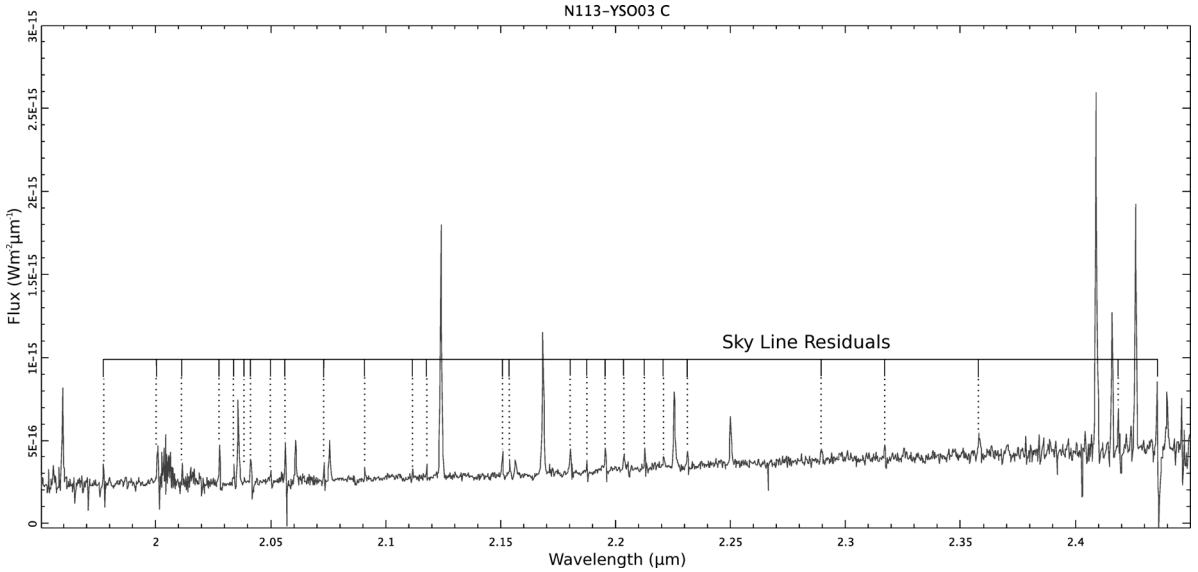

Figure A2. Spectrum of N113-YSO03 C showing the positions of all of the sky line residuals.

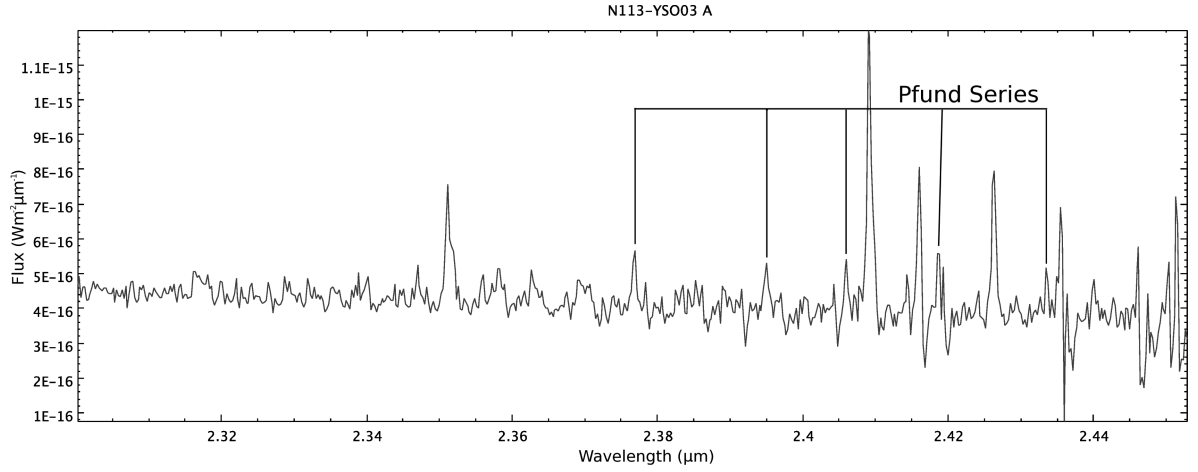

Figure A3. Spectrum of N113-YSO03 A showing the positions of the Pfund series emission lines.

Table B1. Emission line fluxes towards all newly resolved sources. No extinction correction has been applied. Where *p* appears in place of a flux; this denotes that the line is present but the flux cannot be measured.

Object	He I (2.058 μm) (10^{-19} W m^{-2})	Br γ (10^{-19} W m^{-2})	H_2 1–0S(0) (10^{-19} W m^{-2})	H_2 1–0S(1) (10^{-19} W m^{-2})	H_2 1–0S(2) (10^{-19} W m^{-2})	H_2 1–0S(3) (10^{-19} W m^{-2})
N113-YSO01	1.92 ± 0.25	2.00 ± 0.13	0.27 ± 0.26	0.73 ± 0.18	0.41 ± 0.30	
N113-YSO03 A	37.4 ± 2.2	53.8 ± 2.4	1.67 ± 0.30	3.66 ± 0.50	1.19 ± 0.20	1.30 ± 0.41
N113-YSO03 B	6.56 ± 0.35	33.8 ± 1.4	3.02 ± 0.49	7.18 ± 0.49	1.92 ± 0.34	1.37 ± 0.34
N113-YSO03 C	1.53 ± 0.20	7.70 ± 0.38	3.64 ± 0.30	11.7 ± 6.1	3.47 ± 0.36	4.09 ± 0.50
N113-YSO04 A	2.22 ± 0.15	2.66 ± 0.19	0.20 ± 0.03	0.56 ± 0.08	0.19 ± 0.05	
N113-YSO04 B	17.1 ± 1.0	21.1 ± 1.4	0.56 ± 0.12	1.74 ± 0.17	0.75 ± 0.24	

Object	H_2 2–1S(1) (10^{-19} W m^{-2})	H_2 2–1S(2) (10^{-20} W m^{-2})	H_2 2–1S(3) (10^{-19} W m^{-2})	1–0Q(1) (10^{-19} W m^{-2})	1–0Q(2) (10^{-19} W m^{-2})	1–0Q(3) (10^{-19} W m^{-2})
N113-YSO01	0.36 ± 0.08	1.36 ± 0.63		0.94 ± 0.18	1.09 ± 0.10	0.83 ± 0.13
N113-YSO03 A	1.25 ± 0.18	5.53 ± 1.29	1.18 ± 0.22	7.47 ± 0.87	3.14 ± 0.57	3.39 ± 0.27
N113-YSO03 B	1.38 ± 0.14	4.65 ± 0.97	1.42 ± 0.16	12.2 ± 1.0	5.34 ± 0.44	6.93 ± 0.54
N113-YSO03 C	2.04 ± 0.21	6.67 ± 0.85	1.85 ± 0.14	16.5 ± 1.4	6.33 ± 0.56	11.3 ± 0.6
N113-YSO04 A	0.16 ± 0.02	0.93 ± 0.27	0.11 ± 0.03	1.47 ± 0.19	0.69 ± 0.15	0.85 ± 0.07
N113-YSO04 B	0.78 ± 0.11	3.46 ± 1.00	0.62 ± 0.09	3.72 ± 0.45	2.07 ± 0.19	2.11 ± 0.16

Object	He I (2.113 μm) (10^{-20} W m^{-2})	Pf 20-5 (10^{-20} W m^{-2})	Pf 21-5 (10^{-20} W m^{-2})	Pf 22-5 (10^{-20} W m^{-2})	Pf 23-5 (10^{-20} W m^{-2})	Pf 25-5 (10^{-20} W m^{-2})
N113-YSO01						
N113-YSO03 A	9.1 ± 1.6	22.1 ± 8.5	*p*	9.4 ± 2.0	9.3 ± 1.7	10.1 ± 1.3
N113-YSO03 B			13.9 ± 4.3		4.8 ± 1.2	6.7 ± 1.0
N113-YSO03 C						
N113-YSO04 A	2.4 ± 0.5					
N113-YSO04 B	5.8 ± 1.1		8.1 ± 2.4	5.3 ± 1.3	5.2 ± 1.9	3.6 ± 0.9

APPENDIX B: EMISSION-LINE FLUXES

Here, we present the complete set of measured emission-line fluxes obtained and analysed in Section 4.3. These fluxes have not been corrected for extinction and have been obtained by fitting Gaussian profiles to 1D spectra extracted from the regions shown in Fig. 2.

APPENDIX C: SKY LINE VELOCITY MAPS

Here, we present emission-line centroid velocity maps for sky line emission as measured from the sky offset for N113-YSO03. The emission lines measured were chosen because they are relatively strong and cover a relatively large wavelength baseline encompassing all of the emission lines for which we have measured velocity profiles in Section 4.3. Within uncertainties there are no systematic velocity shifts across the detector.

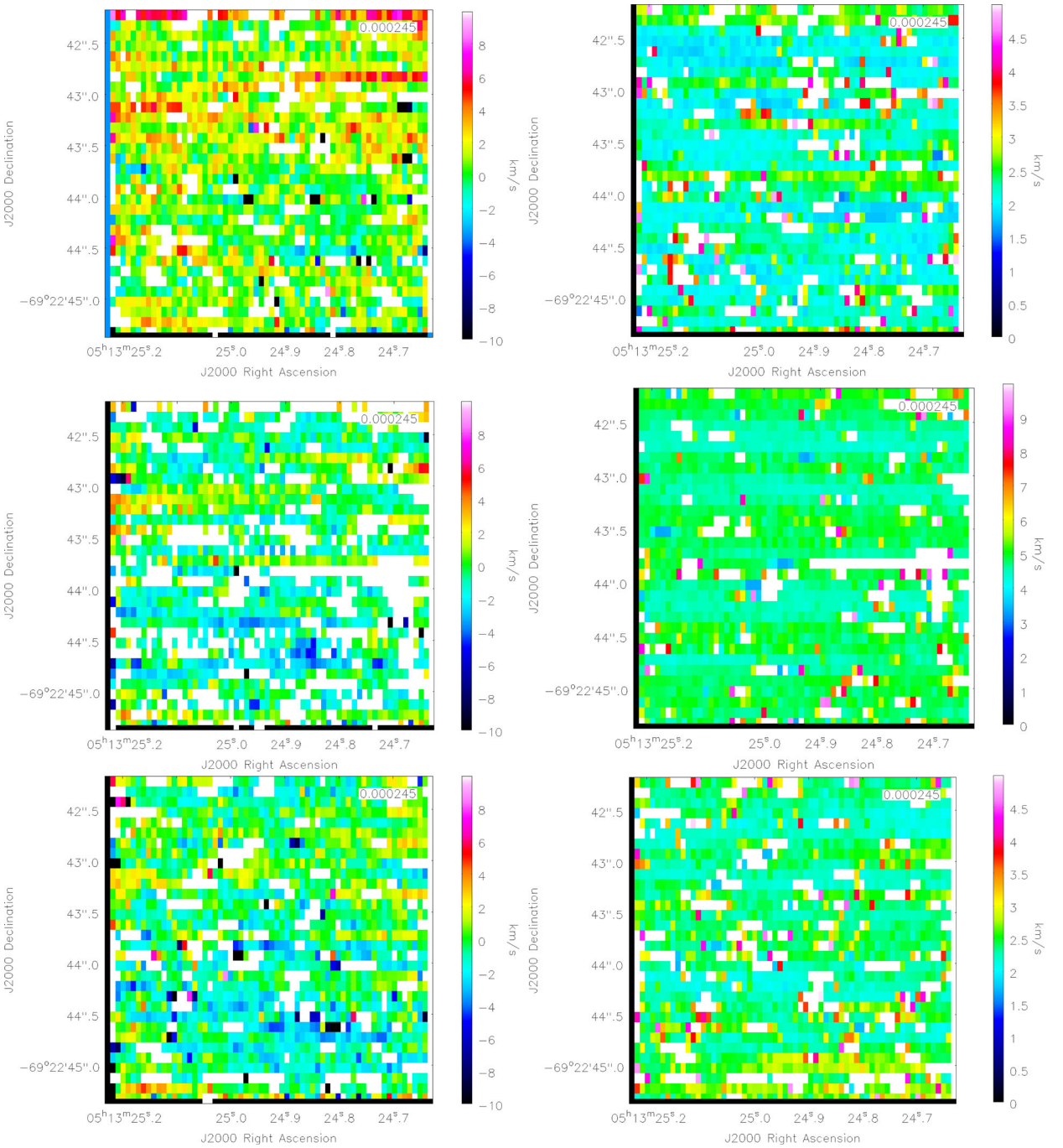

Figure C1. Relative velocity (left) and error maps (right) for sky emission lines in the N113-YSO03 sky cube. Top: 2.0567 μm; middle: 2.1511 μm; bottom: 2.1806 μm.

This paper has been typeset from a TEX/LATEX file prepared by the author.